nature communications

Article

https://doi.org/10.1038/s41467-025-56886-8

Tunneling-barrier-controlled sensitive deep ultraviolet photodetectors based on van der Waals heterostructures

Received: 16 September 2024

Accepted: 5 February 2025

Published online: 05 March 2025

Check for updates

Xiang Li[1,2,3,9], Ziqing Li[1,2,9], Jinhan Hu[1,2,4], Bangchi Huang[1,2], Jianlin Shi[1,2], Zhipeng Zhong[1,2], YeZhao Zhuang[1,2], Yan Chen[1], Jingli Wang[5], Jianfeng Li[4], Lei Zhang[3], Xiangjian Meng[6], Wu Shi[2,7], Shiyou Chen[8], Xiaosheng Fang[1,2] ✉, Hai Huang[1,2] ✉, Jianlu Wang[1,5] ✉ & Junhao Chu[1,6]

Deep ultraviolet (DUV) photodetection usually relies on wide-bandgap semiconductors, which however face challenges in material growth and doping processes. In this work, we proposed and validated a photodetection scheme based on tunneling barrier modulation, achieving highly sensitive DUV photodetection. Using a two-dimensional van der Waals heterostructure, the device integrates MoS_2 as the transporting layer for its high carrier mobility and low dark current, few-layered graphene (FLG) as the photon absorption layer, and hexagonal boron nitride (hBN) as the dielectric barrier. The device exhibits an photoresponsivity of 4.4×10^6 A·W^{-1} and specific detectivity of 1.4×10^{17} cm · Hz$^{-1/2}$ · W^{-1} for 250 nm DUV light, with a rejection ratio R_{250}/R_{450} exceeding 10^6 for visible light. Unlike conventional photodetectors, the cutoff wavelength is determined by the tunneling barrier rather than the material bandgap. Additionally, this photodetection scheme has been extended to a wide range of materials, utilizing different charge transporting layer (e.g., MoS_2, ReS_2), barrier layer (e.g., hBN, Al_2O_3), and photon absorption materials (e.g., FLG, $PdSe_2$, Au, Pd), showcasing its broad adaptability and potential for extensive application. Furthermore, the device has been successfully employed as a power meter for weak UV radiation (0.1 μW·cm^{-2}) and for measuring solar UV irradiance with results matching the meteorological agency's weather reports. Overall, this work introduces an effective approach for developing high-performance DUV photodetectors, highlighting significant potential for applications in the optoelectronic market.

Photodetectors, which convert the optical signal into electrical information, are widely used in optical communication, environmental monitoring, healthcare, and various other fields[1–4], resulting in significant market demand. Many efforts have been made to improve the responsivity and detectivity of photodetectors operating at different wavelengths. In general, the performance of a photodetector relies on multiple factors, involving the photon absorption, photoelectron generation, and charge transport processes[5]. While the photon absorption and photoelectron generation are predominantly determined by the band structure of the absorptive material, charge transport is influenced not only by the electronic structure but also by the material quality, including defects and chemical doping levels. In the case of most detectors, such as photoconductors, photodiodes, these processes occur within a single material[6]. However, the

A full list of affiliations appears at the end of the paper. ✉e-mail: xshfang@fudan.edu.cn; huangh@fudan.edu.cn; jianluwang@fudan.edu.cn

optimization of various factors, including spectral response, quantum efficiency, photogain, and dark current within a single material remains a challenge[7–9], which limits the performance of photodetectors. For instance, in the pursuit of high-performance deep ultraviolet (DUV) photodetection, conventional semiconductor materials with excellent optoelectronic properties, such as silicon, and gallium arsenide, have become unsuitable due to the diminished absorption coefficient in DUV region. Ultrawide bandgap semiconductors, like Ga_2O_3[10–16], diamond[17–20], AlGaN[21–26], have emerged as promising candidates for DUV photodetection, given their high absorption coefficients and effective spectral selection capabilities. Nonetheless, due to the challenges in material growth and chemical doping, their electrical performance still falls short, leading to a large dark current[11] and the obvious defect-related persistent photoconductivity[13,27,28]. They still have a long way to go for the real applications. As a result, the development of high-performance DUV photodetector is still constrained due to the difficulty in optimizing both the optical absorption and electrical transport properties.

To address this challenge, we propose a photodetection device structure formed by distinct and separated photon absorption layer and charge transporting layer. Under this scheme, we could avoid the difficulty of optimizing all the properties in single material. Furthermore, the separation of the charge transport layer from photon absorption layer could extend the lifetime of the photogenerated carries, resulting in a significant increase in photogain. Moreover, through the engineering of tunneling barrier between different layers, we could realize the DUV photodetection using a conventional semiconductor instead of the wide bandgap semiconductor.

In this article, we demonstrated such a tunneling barrier engineered DUV photodetector using emerging two-dimensional (2D) semiconductors heterostructure, wherein the transition metal dichalcogenides (TMDC), such as MoS_2 and ReS_2, are employed as the charge transport layer due to their high carrier mobility until few-layer limit, and FLG, $PdSe_2$, and metallic thin film Au, and Pd are utilized for UV photon absorptance. By introducing a dielectric barrier layer (e.g., hBN, Al_2O_3) to control the barrier height between the photon absorption layer and charge transport layer, we achieved excellent spectra selectivity for UVB to UVC photodetection, with a tunable cutoff wavelength from 440 to 300 nm, and ultrahigh spectra rejection ratio. The MoS_2/hBN/FLG device achieved ultrahigh photoresponsivity (4.4×10^6 A·W^{-1}) and specific detectivity (1.4×10^{17} cm · Hz$^{-1/2}$ · W^{-1}) for 250 nm UV light at an intensity of 1 μW·cm^{-2}, which is superior to most of photodetectors based on wide bandgap semiconductors. In addition, the detector can function as a UV power meter, showing the capability of measuring the weak light down to 0.1 μW·cm^{-2} at 254 nm, outperforming the commercial UV power meter. It has been used to measure the UV irradiance of solar light with results aligning well with the Meteorological agency's weather report. Ultimately, we packaged the device with commercial TO-39 with a lens cap, enhancing its sensitivity and response speed. Therefore, this work opens up a way for developing high performance UV photodetector with general materials, holding the significant potential for future market applications.

Results and discussion

Design of tunneling-barrier-controlled photodetector

In conventional semiconducting photodetectors, such as photoconductors and photodiodes, the photon absorption and charge transport process are combined together in a single material, as shown in Fig. 1a. The spectra response is primarily determined by the photon absorption characteristics of the channel material. Incident photons with energy larger than the bandgap generate the electrons and holes through the internal photoelectric effect, which are then separated by the build-in electric field or the photothermoelectric effect. Subsequently, electrons and holes move in opposite directions under the bias electric field, making them prone to recombination, thereby impacting the device's photogain. Herein, we proposed a tunneling barrier engineered device scheme that separates the photon absorption and charge transport into two distinct layers, as shown in Fig. 1b. Under this scheme, the photon excited electrons or holes in the absorption layer could tunnel through the barrier layer in between, resulting in the regulation of carrier density in the charge transport layer through capacitance coupling. Since there is only one-type of carrier in the charge transport layer, and they move in the same direction under the bias electric field, the recombination rate is significantly reduced, resulting in a substantial increase in photogain.

Furthermore, since the tunneling probability of electron (hole) is determined by the effective barrier height, only the photons with energy greater than the barrier height φ_e (φ_h) could significantly induce the escape of electrons (holes) from the absorption layer, as illustrated in Fig. 1c. Therefore, the device has a spectral response selectivity relying on the barrier height instead of the bandgap of absorption layer, as shown in Fig. 1d. This scheme allows us to adjust

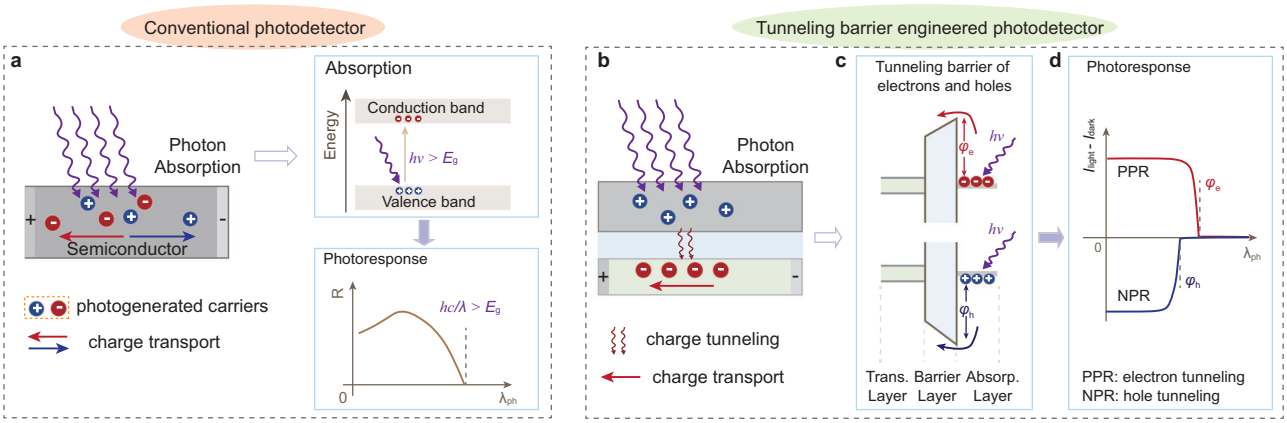

Fig. 1 | Proposed photodetector design. a The conventional photodetector combining the photon absorption and charge transport in single material, the photon absorption and spectra response strongly rely on the bandgap (E_g) of the semiconducting material. $h\nu$ and λ indicates the photon energy and wavelength of the incident photons, c indicates the speed of light. **b** The proposed tunneling barrier engineered device, where the photon absorption and charge transport are separated by a dielectric layer in between. **c** The schematic of tunneling barrier for the electrons and holes in the device. Carriers could tunnel out the barrier layer under the UV light irradiation, when the photon energy is larger than the barrier height of φ_e or hole (φ_h). **d** The spectral response of the positive photoresponse (PPR) and negative photoresponse (NPR) induced by the electron and hole tunneling, respectively. The cutoff wavelength is determined by the height of tunneling barrier.

the spectra response by controlling the barrier height without changing the absorption material. Moreover, taking the n-type charge transport layer as an example, when electrons are excited out the absorption layer, the potential in the absorption layer increases, causing an increase of the electron density in the transport layer, resulting in a positive photoresponse (PPR). Conversely, when the holes are excited out the absorption layer, it causes a reduction of the potential within the absorption layer, which results in a decrease of the electron density in the transport layer, leading to a negative photoresponse (NPR).

DUV photodetector based on 2D heterostructures

Based on the concept, we constructed such a photodetector using the 2D van der Waals materials. In this device, we employed the well-studied TMDC material, MoS_2[29–31], as the charge transport layer, and FLG serves as the photon absorption layer due to its broadband photoresponse. Few-layered hBN acted as the dielectric barrier layer in between. The heterostructure was fabricated using the dry-transfer method on a Si/SiO_2 substrate (see method section for details). The schematic structure of the device is shown in Fig. 2a, and the optical image of the device is shown in Fig. 2b. The thickness of FLG, hBN, and MoS_2, are approximately 10 nm, 13 nm, and 4 nm, respectively, as determined through the atomic force microscopy (Supplementary Fig. 1 and Fig. 2). The flat band alignment of the device is shown in Fig. 2c, in which the FLG layer has an work function of ~4.6 eV[32], is caught in between the hBN and SiO_2 layer. Since the thickness of the barrier layer (hBN) is larger than 4 nm, direct tunneling is negligible. The tunneling of electron (hole) through the barrier layer is controlled by the electric field (Fowler-Nordheim tunneling (FNT)), or the photon excitation[33–35]. The effective barrier height for electron (hole) tunneling is determined by the electron affinity difference of hBN and FLG, as well as the electric field induced band tilting in hBN layer.

Taking advantage of the SiO_2 backgate, the MoS_2 layer can be regulated into either an accumulation or depletion state through a pulsed gate-voltage, corresponding to the low resistance state (LRS) and high resistance state (HRS)[36–38], as shown in Fig. 2d. When a positive gate-voltage pulse is applied, electrons are injected and stored in the FLG layer, creating a negative potential in FLG, which results in the HRS of the MoS_2 channel, as illustrated in Fig. 2e. Conversely, when a negative gate-voltage pulse is applied, holes are injected and stored in

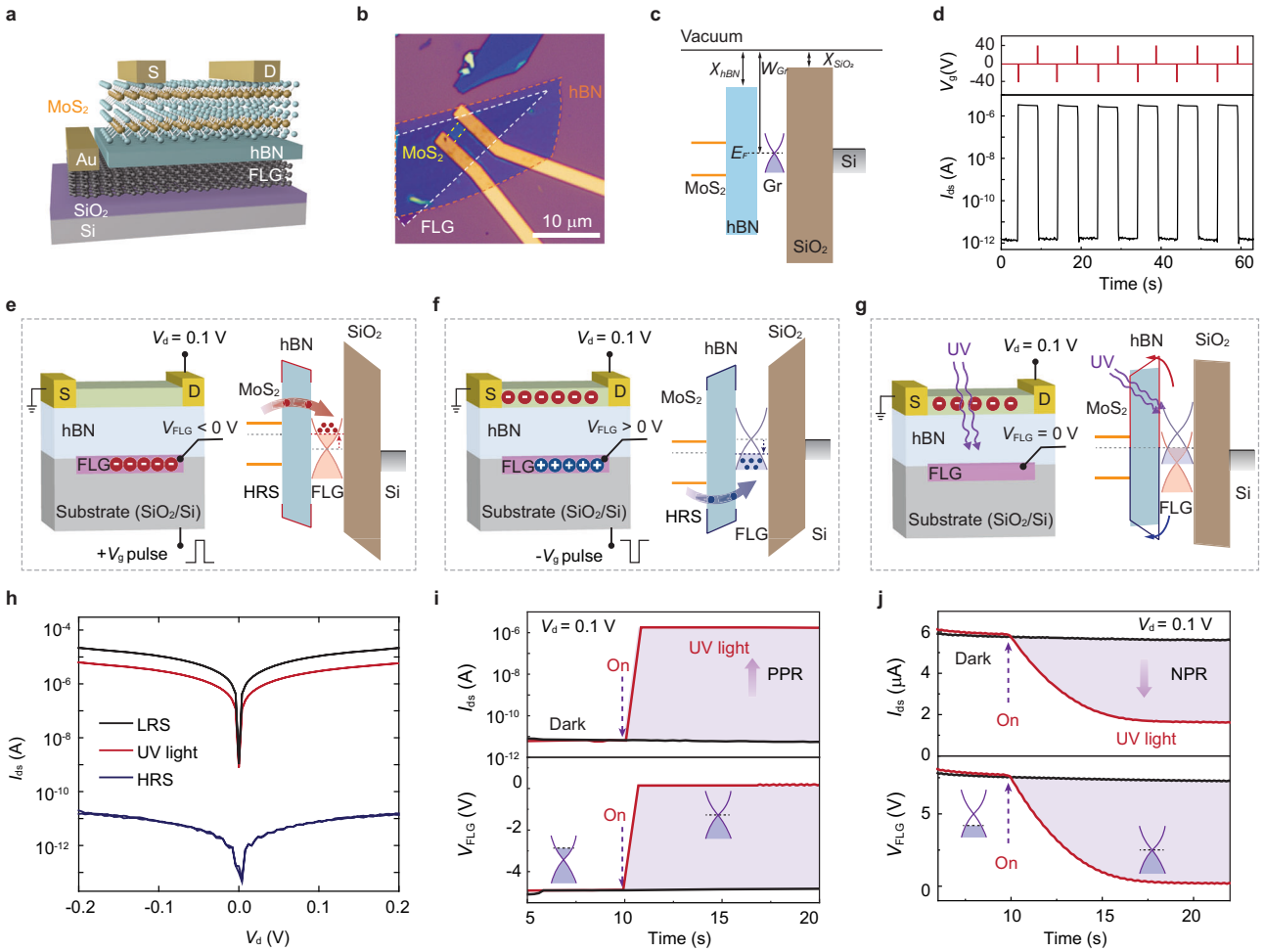

Fig. 2 | Structure and photoresponse mechanism of MoS_2 based device. a The schematic structure of the device. **b** The optical image of MoS_2 based device on Si/SiO_2 substrate, scale bar represents 10 μm, the white dashes indicate the boundary of the few-layered-graphene (FLG) layer, the orange dashes indicate the boundary of the hexagonal Born Nitride (hBN) layer. **c** The flat band diagram of the device. The χ_{hBN} (-2.0 eV) and χ_{SiO2} (-1.0 eV) indicated the electron affinity of the hBN and SiO_2 layer. The W_{Gr} (-4.6 eV) indicates the work function of the FLG layer. E_F denotes the fermi surface of the FLG layer. **d** The current states controlled by backgate voltage (V_g) pulse (width 100 μs) in the dark. The schematic configuration of the charges in the FLG and MoS_2 layer after positive V_g pulse (**e**), negative V_g pulse (**f**), and under UV irradiation (**g**), the electric potential of the FLG layer becomes negative ($V_{FLG} < 0$), positive ($V_{FLG} > 0$), and zero ($V_{FLG} = 0$) correspondingly. **h** Three different conducting states of MoS_2 layer: high resistance state (HRS) after positive V_g pulse, low resistance state (LRS) after negative V_g pulse and photo conducting states under 254 nm UV light irradiation. The PPR (**i**) and NPR (**j**) of the device under 254 nm UV irradiation and the corresponding change in the potential of FLG layer.

https://doi.org/10.1038/s41467-025-56886-8

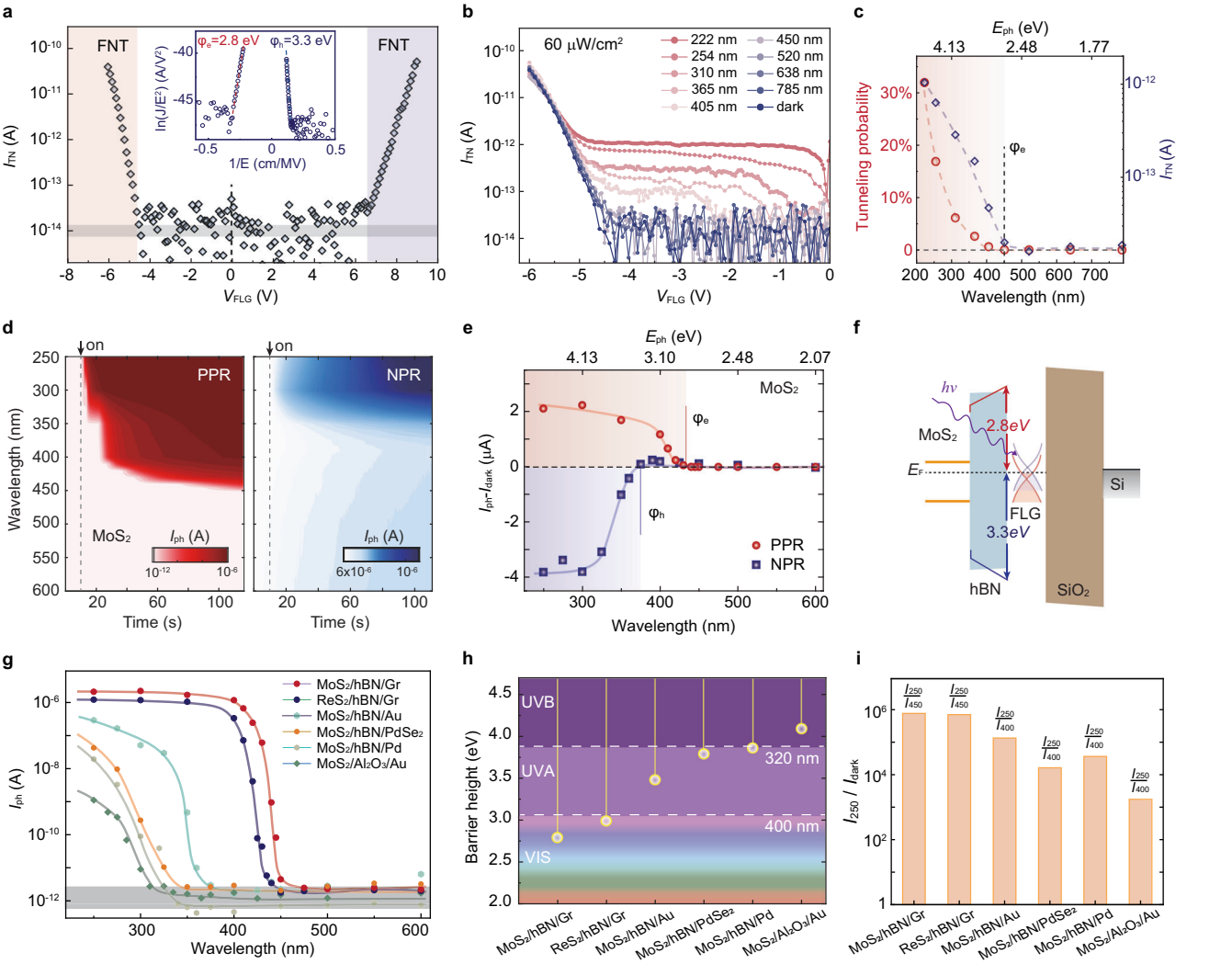

Fig. 3 | Spectral response of tunneling barrier engineered photodetector. a The tunneling current measurement of MoS_2/hBN/FLG device in the dark, and the ln(J/E^2) vs 1/E plot of the tunneling current (inset). The tunneling barrier for electron and hole is 2.8 eV and 3.3 eV, respectively, obtained from the Fowler-Nordheim tunneling (FNT) relationship. **b** Tunneling current curves under illumination with different wavelengths ($P = 60$ μW·cm^{-2}). **c** The tunneling current and probability under different illumination when V_{FLG} is 2 V. **d** Contour image plot of PPR and NPR behavior of MoS_2/hBN/FLG device at varying wavelength from 250 nm to 600 nm. Dashed lines indicate the time light is turned on. PPR is measured at $P = 20$ μW·cm^{-2}, and NPR is measured at $P = 500$ μW·cm^{-2}. **e** Net photocurrent of MoS_2/hBN/FLG device verse wavelength for both PPR and NPR. φ_e and φ_h indicated the cutoff photoenergy. **f** Band diagram of the device under PPR and NPR status. Red and blue arrows indicate the electron and hole tunneling barrier of 2.8 eV, and 3.3 eV, respectively. **g** Spectral response of a series of tunneling barrier engineered devices, with different transporting layer (e.g. MoS_2, ReS_2), barrier layer (e.g. hBN, Al_2O_3), and photon absorption layer (e.g. FLG, $PdSe_2$, Pd, Au). Grey shaded area indicates the dark current of the devices. **h** The barrier height and cut-off wavelengths for the devices. **i** The photocurrent (for 250 nm UV light) to dark current ratio for the devices.

FLG layer, generating a positive potential in the FLG, and leading to the LRS of MoS_2 channel (Fig. 2f). The injected charges remain stored in FLG layer for a long time, maintain the resistance state of the MoS_2 unchanged till exposed to UV light (Supplementary Fig. 3). As depicted in Fig. 2g, under UV illumination, the charges stored in the FLG are excited and tunnel out of the FLG layer, restoring FLG potential to zero. This process alters the electron concentration in the MoS_2 layer, leading to a PPR due to electron tunneling, or a NPR due to hole tunneling. The photoresponse of the MoS_2/hBN/FLG device under 254 nm light irradiation is shown in Fig. 2h, showing the large positive and negative photocurrent comparing with the HRS and LRS state. To confirm the photoresponse is related to the charge tunneling, we directly monitored the voltage potential of FLG layer under UV irradiation together with the resistance changes in the MoS_2 layer. As shown in Fig. 2i, j, the photocurrent increases (decreases) upon the light illumination, and correspondingly the potential of FLG layer increases (decreases) to zero, indicating the charge's tunneling (Supplementary Fig. 4). It's worth to note that the NPR is much slower than the PPR process, this is because the hole tunneling is more difficult than the electron due to its larger effective mass. The variation of the photocurrent relies on the potential change of FLG layer, which can be estimated through the capacitance coupling, as shown in Supplementary Fig. 5.

Furthermore, we have directly measured the tunneling current I_{TN} between FLG and MoS_2 layer in the dark and under light illumination. As shown in Fig. 3a, the electron (hole) tunneling occurs when the voltage is larger than the threshold voltage in the dark, corresponding to the FNT under high electric field. The tunneling barrier height (φ_B) can be extracted from the ln(J/E^2) vs 1/E plot of the tunneling current (inset of Fig. 3a) with the FNT relationship

$$J = \frac{q^3 m_s}{8\pi h m_b \varphi_B} E^2 \exp\left(\frac{-8\pi(2m_b)^{1/2}\varphi_B^{3/2}}{3hq}\frac{1}{E}\right) \quad (1)$$

Where J is the tunneling current density, q is the elementary charge, h is the Plank constant, E is electric field strength in barrier layer, m_b and m_s corresponds to the effective mass of charge in barrier layer and FLG layer, respectively. The effective mass of electron and hole in hBN layer is approximately 0.064, and 0.25 according to previous reports[39]. The tunneling barrier height for electrons and holes is calculated to be 2.8 eV and 3.3 eV, respectively. We also measured the electron tunneling current under light illumination with varying photon energy (light intensity for all wavelength is fixed at 60 μW·cm^{-2}), as shown in Fig. 3b. The tunneling current increases when applied voltage is lower than the FNT threshold, indicating the electron tunneling occurs with the assistance of photon excitation. The tunneling current when V_{FLG} = -3 V are extracted and shown in Fig. 3c. It shows only the photons with energy higher than the tunneling barrier (2.8 eV) could induce significant tunneling current. Moreover, the tunneling probabilities under light illumination are calculated using the formula $T = \frac{\Delta I_{TN}/e}{P \cdot S/h\upsilon}$ where ΔI_{TN} is the net photoinduced tunneling current, and P is power density of light, and S is the effective area of device (overlapping area between MoS_2 and FLG). As it can be seen in Fig. 3c, the electron tunneling probability starts growing up when photon energy larger than 2.8 eV (wavelength shorter than 450 nm), and reaches 32% for 222 nm UV light when V_{FLG} = -3 V. Note that the tunneling probability also depends on the applied voltage due to its impact on the band bending of hBN (Supplementary Fig. 6). Additionally, the tunneling current and photoresponse curve exhibit weak variation when the temperature changes from 100 K to 340 K. This result not only shows the device could work in a broad temperature range, but also rules out the impact of thermal emission on the photoresponse caused by environmental temperature (Supplementary Fig. 7).

With the careful study of the tunneling barrier height between FLG and MoS_2 layer, we further investigated the spectral response of the device from 250 nm to 600 nm. As shown in Fig. 3d, a big contrast of the photoresponse for different wavelength can be seen for both PPR and NPR. The photocurrent of the device dramatically increases from ~10^{-12} A to ~10^{-6} A as the incident light wavelength decreases from 600 nm to 250 nm under weak light irradiation at 20 μW·cm^{-2}. Notably, a large I_{ph}/I_{dark} ratio of 10^6 is achieved. Interestingly, there is almost no photoresponse observed for wavelength longer than 440 nm, despite the photon energy being higher than the bandgap of MoS_2 (1.2–1.8 eV)[30,31]. This suggests that the intrinsic photoconduction effect is nearly negligible under weak light irradiation, and the observed photoresponse at shorter wavelength should not be attributed to the photon absorption in MoS_2 layer (Supplementary Figs. 8–10). Similarly, a large negative photocurrent of 4 μA is observed only for wavelength shorter than 375 nm under 500 μW·cm^{-2}. To highlight the spectral photoresponse, the net photocurrent (I_{ph}-I_{dark}) verse wavelength relationship is displayed in Fig. 3e. The cutoff wavelengths for PPR and NPR are determined as 440 nm and 375 nm, corresponding to the cutoff photon energy of φ_e = 2.8 eV and φ_h = 3.3 eV, respectively. The cut off photon energy is in good agreement with the tunneling barrier height of electron and hole, as extracted through the tunneling current curves, as illustrated in Fig. 3f. The sum of φ_e and φ_h also matches well with the single particle bandgap of hBN[40]. These findings confirm that the photoresponse is driven by the photon-assisted tunneling of electrons or holes in FLG layer. Moreover, the spectral response of the photodetector is determined by the barrier height between the barrier layer (hBN) and absorption layer (FLG), rather than the bandgap of MoS_2 or graphene. We have also excluded the contribution of intrinsic photoelectric effect of hBN, since its different spectral response and finite photocurrent under such weak light illumination (Supplementary Fig. 11).

To confirm the generality of the photodetection scheme, we fabricated a series of heterostructure devices made with different charge transport layer (e.g. MoS_2, and ReS_2), barrier layer (e.g. hBN, and Al_2O_3), and photon absorption layer (e.g. FLG, $PdSe_2$, and metallic thin-film like Au, Pd). For instance, when replacing the charge transporting layer MoS_2 with few-layered ReS_2, another well studied 2D semiconductor with excellent electrical properties[41,42], the device shows similar PPR and NPR photoresponse with the MoS_2/hBN/FLG device (Supplementary Figs. 12 and 13). The cutoff wavelength for the PPR and NPR is approximately 415 nm and 400 nm, corresponding to the electron and hole tunneling barrier of approximately 3.0 eV(φ_e) and 3.1 eV(φ_h), respectively. Note that the value is slightly different from the MoS_2 based device due to the fermi level modulation when FLG is stacked with different materials, where the work function of MoS_2 and ReS_2 differs slightly according to the previous report[43,44]. The sum of φ_e and φ_h is approximately 6.1 eV, which is the same with that of MoS_2/hBN/FLG device.

We have also demonstrated replacing the photon absorption layer with few-layered $PdSe_2$, constructing the structure of MoS_2/hBN/$PdSe_2$ on Si/SiO_2 substrate. The device also shows good spectra selectivity for UVB to UVC photodetection (Supplementary Fig. 14). The cut-off wavelength of MoS_2/hBN/$PdSe_2$ device is shorter (325 nm) than that of MoS_2/hBN/FLG device, since $PdSe_2$ has a larger work function than FLG. Additionally, since the photoresponse mechanism of the device is mainly attributed to the charge storing and photon-assisted electron tunneling process in the photon absorption layer, the FLG layer can also be replaced with thin-film metal, like Au, Pd, forming the device structure of MoS_2/hBN/Au, and MoS_2/hBN/Pd on Si/SiO_2 substrate. In these photodetectors, electrons can also be stored in the thin metal layer (15 nm) with positive gate voltage pulse, and be excited out with the assistance of UV photons, leading to the PPR. The spectral response of these devices can be regulated by the work function of metal thin film. The cut-off wavelength shifted to shorter wave side when changing the Au layer to Pd layer, due to higher work function of Pd leads to the larger electron tunneling barrier (Supplementary Fig. 15). Moreover, we have also demonstrated the hBN barrier layer can be replaced by high quality Al_2O_3 thin film grown by atomic-layer-deposition (ALD) method (Methods and Supplementary Fig. 15). The MoS_2/Al_2O_3/Au on Si/SiO_2 substrate also shows a good spectral selectivity for UV photodetection with a cut-off wavelength of ~300 nm. The spectral response of all the devices made with different charge transport layer, barrier layer, and photon absorption layer are summarized in Fig. 3g. It demonstrates the tunneling barrier engineered photodetection scheme can be widely applicated in a variety of materials. The cut-off wavelength and barrier heights of the devices are summarized in Fig. 3h, showing the tunable spectral response for UV photodetection. The photocurrent (250 nm UV light) to dark current ratio I_{254}/I_{dark} of different devices are shown in Fig. 3i. Since the photocurrent above the cut-off wavelength is almost zero under 20 μW·cm^{-2} light illumination, the I_{254}/I_{dark} ratio nearly equals to the I_{250}/I_{450} or I_{250}/I_{400} in the photodetectors as labeled in Fig. 3i. The I_{250}/I_{450} ratio reaches as high as 10^6 in MoS_2/hBN/FLG photodetector, leading to a larger spectral rejection ratio between UV (250 nm) and visible light (>450 nm).

Performance of the DUV photodetector

Although the NPR working mode also exhibits high photocurrent, but the signal to noise ratio is low due to its high dark current. Therefore, in the photodetection application, we only consider the PPR working mode. We systematically studied the photodetection performance for the UV region. Figure 4a shows the time-resolved photoresponse of MoS_2 based device under 250 nm light irradiation with different power intensities (photoresponse for other wavelengths are shown in Supplementary Fig. 17). The photocurrent increased dramatically after light irradiation, and remained at a high current level until a positive pulse gate voltage (V_g) applied. Note that the magnitude of V_g pulse can be reduced to 10 V for devices on silicon substrate with 285 nm SiO_2, and to 2 V for devices on silicon substrate with 100 nm SiO_2 (Supplementary Fig. 18). The combination of the gate-voltage pulse

https://doi.org/10.1038/s41467-025-56886-8

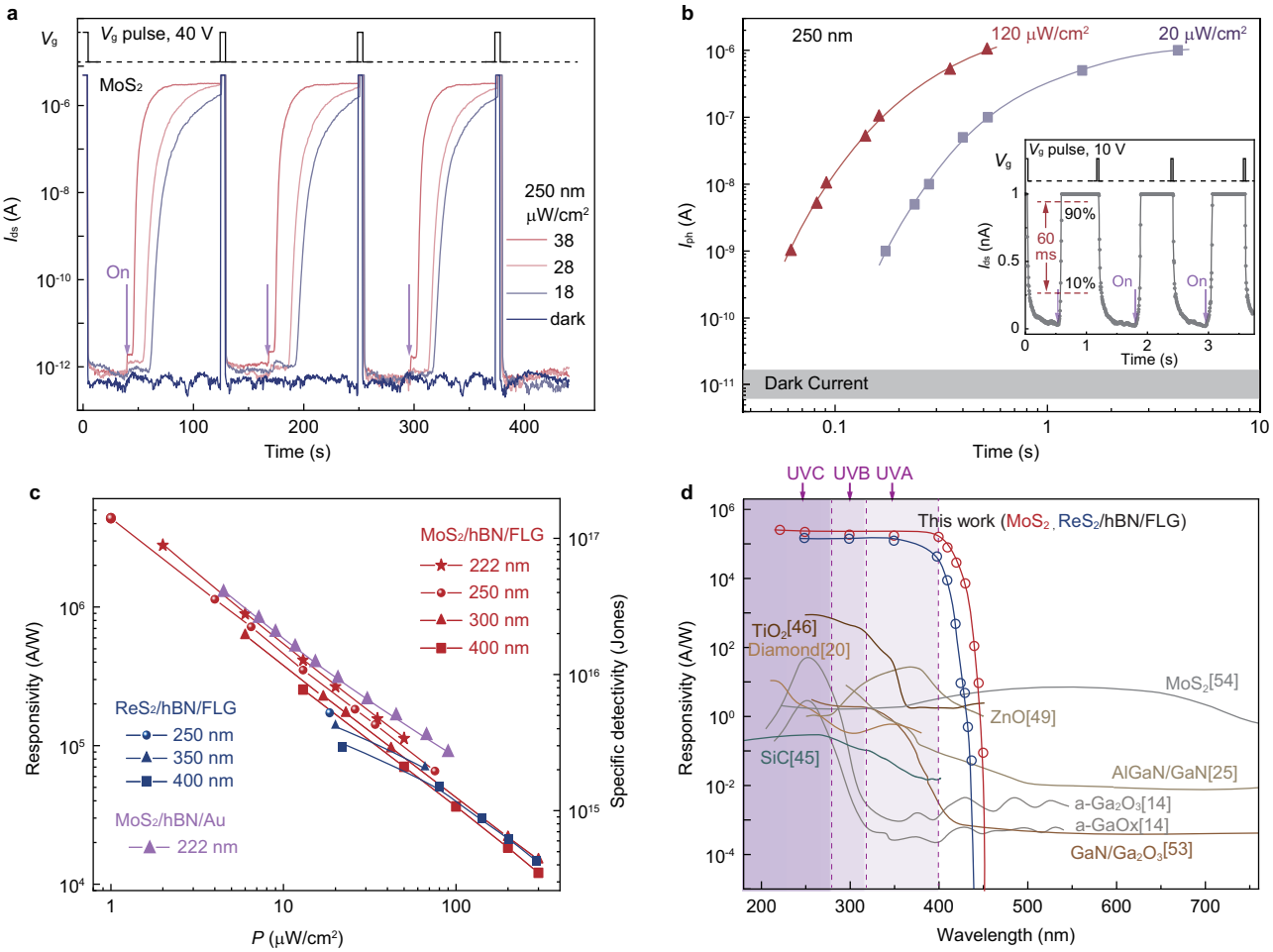

Fig. 4 | Performance of the deep ultraviolet photodetector. a Time resolved photoresponse to the 250 nm UV light at different power density (V_{ds} = 0.1 V). A gate voltage pulse is used to reset the device to high resistance state after each light pulse. **b** The relationship of photocurrent and response time, triangle and square symbols represent the data measured under 120 μW·cm^{-2} and 20 μW·cm^{-2}, respectively, grey shaded area indicate the dark current of the device. The inset shows a response time of 60 ms when the compliance current is 10^{-9} A. **c** Photoresponsivity and specific detectivity of MoS_2/hBN/FLG, ReS_2/hBN/FLG, and MoS_2/hBN/Au devices at varying wavelengths. **d** Comparison of the photoresponsivity among the UV photodetectors made with wide bandgap semiconductors. The MoS_2/hBN/FLG, ReS_2/hBN/FLG devices are measured with 0.1 V bias voltage, with light intensity of 20 μW·cm^{-2}, the other experimental conditions are listed in Supplementary Table 1.

enabled the continuous operation of the photodetector with the accumulation time determined by the interval between two gate-voltage pulses. Additionally, the response time of the device can be adjusted by tuning the compliance current. As shown in Fig. 4b, when the compliance current is set to 10^{-9} A, the device shows a fast photoresponse of 60 ms to 254 nm UV light with an intensity of 120 μW·cm^{-2}, while maintaining an I_{ph}/I_{dark} ratio of nearly 10^3 (The relationship between compliance current and response time are shown in Supplementary Fig. 19).

The device not only shows high photocurrent, but also processes low current noises. The current noise power spectra were measured through the noise analyzer at different bias voltage (Supplementary Fig. 20). We calculated the photoresponsivity using the formula $R = (I_{ph} - I_{dark})/P$, where P is the intensity of light shining on the device area. The specific detectivity is calculated using $D^* = (R \cdot \sqrt{A})/i_n$, where A is the effective area of the device (overlapping area between MoS_2 and FLG layer in this device is measured to be 40 μm^2, see Supplementary Fig. 21), and i_n is the noise spectral density calculated using the formula[7] $\left\langle i_n^2 \right\rangle = \frac{1}{B}\int_0^B S_n(f)df$. The photoresponsivity and detectivity of both the MoS_2/hBN/FLG and ReS_2/hBN/FLG photodetector as a function of wavelength and power density is shown in Fig. 4c. It shows both the responsivity and detectivity increases at shorter wavelengths, reaching 4.4 × 10^6 A·W^{-1} and 1.4 × 10^{17} cm · Hz$^{-1/2}$ · W^{-1} for the DUV light (250 nm, P = 1 μW·cm^{-2}), respectively. The photogain, G = (R ηhc)/$e\lambda$, is estimated to be as high as 2.2 × 10^7, when the external quantum efficiency η is asuumed to be 100%. This high photogain is benefited from the separation of charge transport and photon absorption in this device. Note that the performance has been stablely achieved among different devices, as it is shown in Supplementary Fig. 22. In addition, we also demonstrated the package of the MoS_2/hBN/FLG device using the transistor outline (TO-39) with quartz lens (Supplementary Fig. 23). Since the UV light can be focused by the quartz lens, resulting in the enhanced power density illuminated on the device. The response speed can be improved by 7 times in this packgaed device, yielding a response time (photocurrent increase from 10% to 90% of the saturation current) of 70 ms for 254 nm UV light of 300 μW·cm^{-2} with an I_{ph}/I_{dark} ratio of 10^6.

To further demonstrate the performance of the device, We made a comparison of the responsivity and detectivity with other UV detectors (Fig. 4d and Supplementary Table 1). The device shows ultrahigh photoresponsivity comparing with many other UV photodetectors for DUV light, such as those made with AlGaN pin

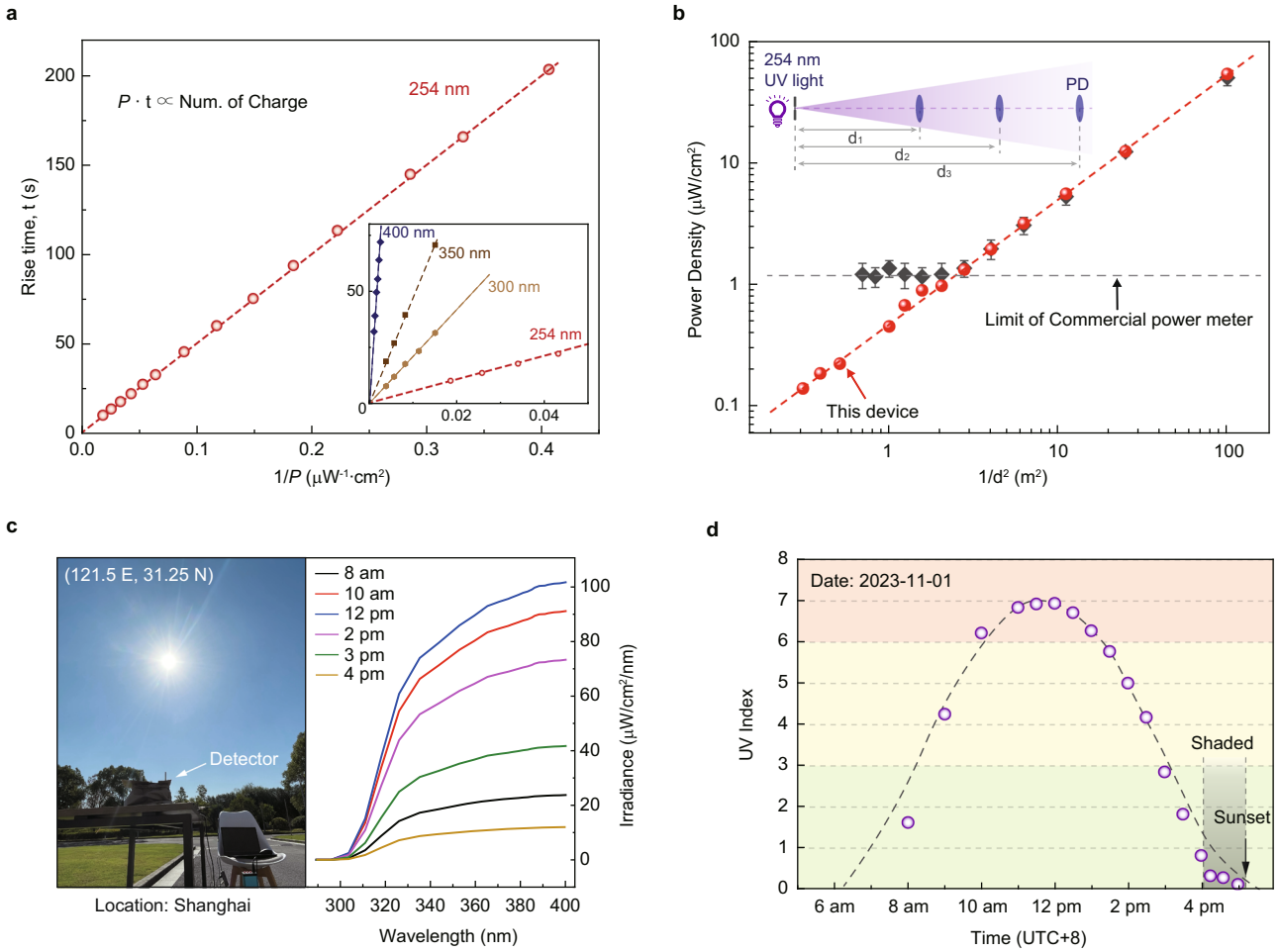

Fig. 5 | Power meter application of the MoS_2/hBN/FLG device. a The inverse proportional relationship between rising time and power density of 254 nm light (red symbol). Inset shows the relationship for 300 nm (yellow symbol), 350 nm (brown symbol), and 400 nm (blue symbol) light. Dashed lines are linear fit to the data. **b** The power intensity of UV disinfection lamp at varying distance measured by the MoS_2 based device (red circles) and the commercial power meter (dark diamonds). The error bar represents one standard deviation of the power intensity measured over multiple times. Inset shows the schematic configuration of the experiment, d_1, d_2, d_3 show the varying distance between light source and photodetector. **c** The photograph of measuring the sunlight UV radiation with MoS_2/hBN/FLG photodetector and the calibrated UV spectrum (290–400 nm) at different time from 8 am to 4 pm. **d** The calculated UV index at different time on Nov. 1, 2023. The direct sunlight is shaded after 4 pm, as the shaded area indicated. The dashed line is UV index calculated through the history UV irradiation data from http://www.wheata.cn/.

junction[24], a-Ga_2O_3[14], 4H-SiC[45], diamond[20], TiO_2[46–48], ZnO[49,50], and various other wide bandgap semiconductors[51–53]. In particular, the photoresponsivity is significantly higher than the pure MoS_2 device, whose maximum responsivity is observed in the visible regime[54]. This difference in spectral response further confirms that the photoabsorption mechanism in our device differs from the intrinsic absorption properties of MoS_2. Moreover, the MoS_2/hBN/FLG device operates at a low reading voltage of 0.1 V, achieving an ultrahigh on/off ratio of 10^6 in the photocurrent and ultralow dark current of 1 pA. The response time can reach as fast as 60 ms, which is comparable to many UV photodetectors made with wide bandgap materials[12,14,51]. These results affirm that, by employing this structural design, we have succuessfully made a highly sensitive DUV photodetector with general bandgap semiconductors.

Ultrasensitive power meter application

Considering the ultrahigh photoresponsivity, the device could be used for detecting the weak light irradiation from the environment. For instance, we have demonstrated its application in detecting UV radiation from voltaic arc and flames, as shown in Supplementary Fig. 24. Without a doubt, it could also be used for detecting the irradiation from UV counterfeit detection lamp, disinfection lamp and so on (Supplementary Fig. 25). Moreover, since the photocurrent of the MoS_2 layer saturates until the charges stored in the FLG layer are fully excited and tunneling out, i.e. the potential of the FLG layer reaches zero, as shown in Fig. 2e. In this process, the rising time (t) of the photocurrent is inversely proportional to the light intensity (P), and their product (P·t) should be a constant, determined by the number of charges stored in the FLG layer. Indeed, Fig. 5a shows the rising time is proportional to the inverse of power intensity for different wavelengths. The product of P·t also depends on the wavelength of incident light, this is because the tunneling probability is strongly dependent on the excitation photon energy (Fig. 3c). Utilizing this relationship allows us to precisely determine the power intensity of light by counting the time of photocurrent saturation. Therefore, the device could be used as a power meter for UV light.

To test the capability of the device as a power meter, we measured the irradiation of a UV disinfection lamp at varying distance, as illustrated in the inset of Fig. 5b. A narrow slit (about 0.5 cm width) is applied for the UV irradiation to reduce the total intensity, and the detector device is placed at distances from 0.1 m to 1.8 m. By measuring the photocurrent vs time curves under the irradiation

(Supplementary Fig. 26), we could extract the rising time under different measuring condition (i.e. different detector position). Therefore, we calibrated the power intensity of the irradiation as shown in Fig. 5b. The power intensity is inversely proportional to the square of distance between the source and detector. This is in a good agreement with the law of illumination, indicating the accuracy of the calibrated power intensity using our device. Moreover, comparing the power intensity measured through a commercial power meter with our device, we found our device shows much higher resolution down to 0.1 μW·cm^{-2}, than the commercial power meter (OPHIR NOVA II), whose resolution limit is about 1 μW·cm^{-2}. Therefore, these results suggest that our device can be used as an ultrasensitive power meter.

Further applications of our device have been demonstrated by measuring the UV intensity of the sunlight throughout an entire day. Figure 5c shows the experimental setup for assessing environmental UV intensity using our device. To eliminate interference from visible light, a UV low-pass filter was employed. The UV intensity is calibrated through the rising time of photoresponse to sunlight, where the t verse *P* relationships at different wavelengths are accounted (Fig. 5a and Supplementary Fig. 27). The solar irradiance spectrum in the UV region (290–400 nm) at various time is shown in Fig. 5c. Additionally, the UV index, a standard measurement of the strength of the sunburn[55], is calculated considering the erythemal action spectrum (see method and Supplementary Fig. 28). The UV index from 8 am to 5 pm is shown in Fig. 5d. Notably, the experimental results are in good agreement with the values provided by the Meteorological agency. These findings highlight the potential of our device as a sensitive power meter in the environmental monitoring, addressing the urgent needs of both industry and customer electronics.

In conclusion, we have demonstrated a tunneling-barrier-engineered DUV photodetector where the photon absorption and charge transportation are separated in different layers, leading to a significantly improved performance. We verified the photodetection scheme through a series of heterostructure devices with varying charge transport materials (e.g. MoS_2, ReS_2), barrier layer materials (e.g. hBN, Al_2O_3), and photon absorption materials (e.g. FLG, $PdSe_2$, and metallic Au and Pd) on Si/SiO_2 substrate. These devices demonstrate good spectral selectivity for UV photodetection, which is controlled by the tunneling barrier height instead of the bandgap of photon absorption material. The photodetectors, e.g. MoS_2/hBN/FLG, exhibit ultrahigh photoresponsivity and specific detectivity down to 222 nm UV light, which are superior to many devices made with wide bandgap semiconductors. Moreover, the devices show promising capabilities for weak light detection, and can be used as a sensitive UV power meter with high resolution of 0.1 μW·cm^{-2}, surpassing the commercial power meters. We have successfully employed this device to measure the UV irradiance of disinfection lamp and solar light. Ultimately, this work presents a significant advancement in fabricating high-performance DUV photodetectors based on general bandgap semiconductors, overcoming the challenges of developing ultrawide bandgap semiconductors.

Methods

Device fabrication

The multilayered 2D materials (graphene, hBN, MoS_2, ReS_2) were obtained through the mechanical exfoliation method from the bulk crystal (purchased from the HQ graphene). Subsequently, they were transferred to the Si substrate with 285 nm SiO_2 layer. The heterostructure were made with the dry transfer method with polydimethylsiloxane (PDMS) stamp. The graphene layer was initially transferred to the substrate, followed by stacking hBN on the graphene, and finally adding MoS_2 or ReS_2 layer. The heterostructure were annealed at 400 °C for 3 h in an Ar atmosphere. Cr/Au (10/60 nm) electrodes were prepared by standard electron-beam lithography and metal deposition techniques. The high quality Al_2O_3 thin film with a thickness of 15 nm were grown by atomic-layer-deposition (ALD) at 300 °C.

Device characterization and UV index calibration

The electrical properties of the device were characterized using the semiconductor analyzer Keithley 4200A and the Keysight B2912B. The spectra responses were measured with the light source system consisting of an Xe lamp and a monochromator. The thickness of few layered 2D materials were characterized by the atomic force microscopy. For the sunlight photoresponse measurements, the device was directed exposed to the sunlight outdoors throughout an entire day, starting from the morning (8 am) to the afternoon (5 pm). Calibration of the UV intensity of the sun light involves considering the standard solar spectrum in the UV region and the device's response time at different wavelengths (i.e. different photon energies). The electron tunneling coefficient was estimated by the inverse of the product of *P*·t, and its relationship with the incident photon energy was fitted through an exponential function (Supplementary Fig. 27), as the probability of the photon assisted electron tunneling is exponentially related to the photon energy. Calibration of the UV index followed the standard method, involving integration the product of the erythema action spectrum and the UV spectrum, normalized by 2.5 μW·cm^{-2}. Historical meteorological data is accessible from the website: http://www.wheata.cn/.

Data availability

The Source Data underlying the figures of this study are available at https://doi.org/10.6084/m9.figshare.28204334. All raw data generated during the current study are available from the corresponding authors upon request.

References

1. Li, Z., Yan, T. & Fang, X. Low-dimensional wide-bandgap semiconductors for UV photodetectors. *Nat. Rev. Mater.* **8**, 587–603 (2023).
2. Grotevent, M. J. et al. Integrated photodetectors for compact Fourier-transform waveguide spectrometers. *Nat. Photonics* **17**, 59–64 (2023).
3. Lien, M.-B. et al. Ranging and light field imaging with transparent photodetectors. *Nat. Photonics* **14**, 143–148 (2020).
4. Agarwal, H. et al. Ultra-broadband photoconductivity in twisted graphene heterostructures with large responsivity. *Nat. Photonics* **17**, 1047–1053 (2023).
5. Liu, C. et al. Silicon/2D-material photodetectors: from near-infrared to mid-infrared. *Light Sci. Appl.* **10**, 123 (2021).
6. Rogalski, A., Bielecki, Z., Mikołajczyk, J. & Wojtas, J. Ultraviolet Photodetectors: From Photocathodes to Low-Dimensional Solids. *Sensors* **23**, 4452 (2023).
7. Wang, F., Zhang, T., Xie, R., Wang, Z. & Hu, W. How to characterize figures of merit of two-dimensional photodetectors. *Nat. Commun.* **14**, 2224 (2023).
8. Konstantatos, G. Current status and technological prospect of photodetectors based on two-dimensional materials. *Nat. Commun.* **9**, 5266 (2018).
9. Qiu, Q. & Huang, Z. Photodetectors of 2D Materials from Ultraviolet to Terahertz Waves. *Adv. Mater.* **33**, 2008126 (2021).
10. Zhang, Q. et al. Enhanced gain and detectivity of unipolar barrier solar blind avalanche photodetector via lattice and band engineering. *Nat. Commun.* **14**, 418 (2023).
11. Hou, X. et al. High-Performance Harsh-Environment-Resistant GaO_X Solar-Blind Photodetectors via Defect and Doping Engineering. *Adv. Mater.* **34**, 2106923 (2021).
12. Chen, Y. et al. Ultra-sensitive flexible Ga_2O_3 solar-blind photodetector array realized via ultra-thin absorbing medium. *Nano Res.* **15**, 3711–3719 (2021).
13. Kong, W.-Y. et al. Graphene-β-Ga_2O_3 Heterojunction for Highly Sensitive Deep UV Photodetector Application. *Adv. Mater.* **28**, 10725–10731 (2016).

14. Qian, L.-X. et al. Ultrahigh-Responsivity, Rapid-Recovery, Solar-Blind Photodetector Based on Highly Nonstoichiometric Amorphous Gallium Oxide. *ACS Photonics* **4**, 2203–2211 (2017).
15. Han, Y. et al. Ultrahigh Detectivity Broad Spectrum UV Photodetector with Rapid Response Speed Based on p-β Ga_2O_3/n-GaN Heterojunction Fabricated by a Reversed Substitution Doping Method. *Small* **19**, 2206664 (2023).
16. Wu, C. et al. Review of self-powered solar-blind photodetectors based on Ga_2O_3. *Mater. Today Phys.* **28**, 100883 (2022).
17. Chang, X. et al. UV-photodetector based on NiO/diamond film. *Appl. Phys. Lett.* **112**, 032103 (2018).
18. Cheng, L., Wu, Y., Cai, W. & Zheng, W. Diamond immersion photodetector for 213 nm deep-ultraviolet photodetection. *Mater. Today Phys.* **36**, 101164 (2023).
19. Lin, C.-N. et al. High performance diamond-based solar-blind photodetectors enabled by Schottky barrier modulation. *Carbon* **200**, 510–516 (2022).
20. Liu, B. et al. Self-Powered Solar-Blind UV Detectors Based on O-Terminated Vertical Diamond Schottky Diode with Low Dark Current, High Detectivity, and High Signal-to-Noise Ratio. *ACS Appl. Electron. Mater.* **4**, 5996–6003 (2022).
21. Sun, H. et al. Graded-Index Separate Confinement Heterostructure AlGaN Nanowires: Toward Ultraviolet Laser Diodes Implementation. *ACS Photonics* **5**, 3305–3314 (2018).
22. Kneissl, M., Seong, T.-Y., Han, J. & Amano, H. The emergence and prospects of deep-ultraviolet light-emitting diode technologies. *Nat. Photonics* **13**, 233–244 (2019).
23. Cai, Q. et al. Progress on AlGaN-based solar-blind ultraviolet photodetectors and focal plane arrays. *Light Sci. Appl.* **10**, 94 (2021).
24. Collins, C. J. et al. Improved solar-blind detectivity using an $Al_xGa_{1-x}N$ heterojunction p-i-n photodiode. *Appl. Phys. Lett.* **80**, 3754–3756 (2002).
25. Pandit, B., Schubert, E. F. & Cho, J. Dual-functional ultraviolet photodetector with graphene electrodes on AlGaN/GaN heterostructure. *Sci. Rep.* **10**, 22059 (2020).
26. Zhang, Y.-Y. et al. High Performance Flexible Visible-Blind Ultraviolet Photodetectors with Two-Dimensional Electron Gas Based on Unconventional Release Strategy. *ACS Nano* **15**, 8386–8396 (2021).
27. Sui, Y., Liang, H., Huo, W., Wang, Y. & Mei, Z. A flexible and transparent β-Ga_2O_3 solar-blind ultraviolet photodetector on mica. *J. Phys. D* **53**, 504001 (2020).
28. Zhou, H.-T. et al. High-performance high-temperature solar-blind photodetector based on polycrystalline Ga_2O_3 film. *J. Alloys Compd.* **847**, 156536 (2020).
29. Xia, Y. et al. 12-inch growth of uniform MoS_2 monolayer for integrated circuit manufacture. *Nat. Mater.* **22**, 1324–1331 (2023).
30. Lopez-Sanchez, O., Lembke, D., Kayci, M., Radenovic, A. & Kis, A. Ultrasensitive photodetectors based on monolayer MoS_2. *Nat. Nanotechnol.* **8**, 497–501 (2013).
31. Mak, K. F., Lee, C., Hone, J., Shan, J. & Heinz, T. F. Atomically Thin MoS_2: a New Direct-Gap Semiconductor. *Phys. Rev. Lett.* **105**, 136805 (2010).
32. Yu, Y.-J. et al. Tuning the Graphene Work Function by Electric Field Effect. *Nano Lett.* **9**, 3430–3434 (2009).
33. Martín Sabanés, N. et al. Femtosecond Thermal and Nonthermal Hot Electron Tunneling Inside a Photoexcited Tunnel Junction. *ACS Nano* **16**, 14479–14489 (2022).
34. Vu, Q. A. et al. Two-terminal floating-gate memory with van der Waals heterostructures for ultrahigh on/off ratio. *Nat. Commun.* **7**, 12725 (2016).
35. Vu, Q. A. et al. Tuning Carrier Tunneling in van der Waals Heterostructures for Ultrahigh Detectivity. *Nano Lett.* **17**, 453–459 (2017).
36. Wu, L. et al. Atomically sharp interface enabled ultrahigh-speed nonvolatile memory devices. *Nat. Nanotechnol.* **16**, 882–887 (2021).
37. Liu, L. et al. Ultrafast non-volatile flash memory based on van der Waals heterostructures. *Nat. Nanotechnol.* **16**, 874–881 (2021).
38. Huo, N. & Konstantatos, G. Ultrasensitive all-2D MoS_2 phototransistors enabled by an out-of-plane MoS_2 PN homojunction. *Nat. Commun.* **8**, 572 (2017).
39. Zhou, S. et al. Optical-Field-Driven Electron Tunneling in Metal–Insulator–Metal Nanojunction. *Adv. Sci.* **8**, 2101572 (2021).
40. Cassabois, G., Valvin, P. & Gil, B. Hexagonal boron nitride is an indirect bandgap semiconductor. *Nat. Photonics* **10**, 262–266 (2016).
41. Tongay, S. et al. Monolayer behaviour in bulk ReS_2 due to electronic and vibrational decoupling. *Nat. Commun.* **5**, 3252 (2014).
42. Rahman, M., Davey, K. & Qiao, S.-Z. Advent of 2D Rhenium Disulfide (ReS_2): Fundamentals to Applications. *Adv. Funct. Mater.* **27**, 1606129 (2017).
43. Lee, S. Y. et al. Large Work Function Modulation of Monolayer MoS_2 by Ambient Gases. *ACS Nano* **10**, 6100–6107 (2016).
44. Shim, J. et al. Phosphorene/rhenium disulfide heterojunction-based negative differential resistance device for multi-valued logic. *Nat. Commun.* **7**, 13413 (2016).
45. Zhang, R. et al. A dual P-layer 4H-SiC p-i-n photodetector for the detection from extreme ultraviolet to ultraviolet-A. *Electron. Lett.* **59**, 12953 (2023).
46. Kong, X. et al. Metal-semiconductor-metal TiO_2 ultraviolet detectors with Ni electrodes. *Appl. Phys. Lett.* **94**, 123502 (2009).
47. Li, Z., Li, Z., Zuo, C. & Fang, X. Application of Nanostructured TiO_2 in UV Photodetectors: A Review. *Adv. Mater.* **34**, 2109083 (2022).
48. Xu, X. et al. A Real-Time Wearable UV-Radiation Monitor based on a High-Performance p-CuZnS/n-TiO_2 Photodetector. *Adv. Mater.* **30**, 1803165 (2018).
49. Zheng, M. et al. ZnO ultraviolet photodetectors with an extremely high detectivity and short response time. *Appl. Surf. Sci.* **481**, 437–442 (2019).
50. Jin, Z. et al. Graphdiyne: ZnO Nanocomposites for High-Performance UV Photodetectors. *Adv. Mater.* **28**, 3697–3702 (2016).
51. Qu, Y. et al. Enhanced Ga_2O_3/SiC ultraviolet photodetector with graphene top electrodes. *J. Alloys Compd.* **680**, 247–251 (2016).
52. Dahal, R., Al Tahtamouni, T. M., Fan, Z. Y., Lin, J. Y. & Jiang, H. X. Hybrid AlN–SiC deep ultraviolet Schottky barrier photodetectors. *Appl. Phys. Lett.* **90**, 263505 (2007).
53. Guo, D. et al. Self-Powered Ultraviolet Photodetector with Superhigh Photoresponsivity (3.05 A/W) Based on the GaN/Sn:Ga_2O_3 pn Junction. *ACS Nano* **12**, 12827–12835 (2018).
54. Wang, H. et al. Extremely Low Dark Current MoS_2 Photodetector via 2D Halide Perovskite as the Electron Reservoir. *Adv. Opt. Mater.* **8**, 1901402 (2020).
55. Zou, W. et al. Skin color-specific and spectrally-selective naked-eye dosimetry of UVA, B and C radiations. *Nat. Commun.* **9**, 3743 (2018).

Acknowledgements

This work is supported by the National Key Research and Development Program of China (Grants No. 2021YFB2012601 (H.H.) and 2021YFA1200700(J.W.)), National Natural Science Foundation of China (grants No. 12204109(H.H.)), Science and Technology Innovation Plan of Shanghai Science and Technology Commission (grant No. 21JC1400200(H.H.)), Higher Education Industry Support Program of Gansu Province (grant No. 2022CYZC-06 (L.Z.)). Part of the experimental work has been carried out in Fudan Nanofabrication Laboratory.

Author contributions

X.L., Z.L., J.H., B.H, J.S., Z.Z., Y.Z., and JingLi W. fabricated the devices and conducted the optoelectronic characterization. X.L., Z.L., Y.C., W.S., and H.H. analyzed the experimental data. J.L., L.Z., X.M., S.C., X.F., Jianlu W. and J.C. advised on the experiments and data analysis. X.L., H.H. wrote the manuscript based on inputs from all the other authors. H.H. and J.W. conceived this project.

Competing interests
The authors declare no competing interests.

Additional information
Supplementary information The online version contains supplementary material available at https://doi.org/10.1038/s41467-025-56886-8.

Correspondence and requests for materials should be addressed to Xiaosheng Fang, Hai Huang or Jianlu Wang.

Peer review information *Nature Communications* thanks the anonymous reviewers for their contribution to the peer review of this work. A peer review file is available.

[1]State Key Laboratory of Photovoltaic Science and Technology, Shanghai Frontiers Science Research Base of Intelligent Optoelectronic and Perception, Institute of Optoelectronic and Department of Materials Science, Fudan University, Shanghai, China. [2]Zhangjiang Fudan International Innovation Center, Fudan University, Shanghai, China. [3]School of Mathematics and Physics, Lanzhou Jiaotong University, Lanzhou, China. [4]School of Materials Science and Engineering, Lanzhou Jiaotong University, Lanzhou, China. [5]State Key Laboratory of Integrated Chips and Systems, Frontier Institute of Chip and System, Fudan University, Shanghai, China. [6]State Key Laboratory of Infrared Physics, Shanghai Institute of Technical Physics, Chinese Academy of Sciences, Shanghai, China. [7]State Key Laboratory of Surface Physics and Institute for nanoelectronic devices and quantum computing, Fudan University, Shanghai, China. [8]Key Laboratory of Computational Physical Sciences (MOE), and State Key Laboratory of ASIC and System, School of Microelectronics, Fudan University, Shanghai, China. [9]These authors contributed equally: Xiang Li, Ziqing Li. ✉e-mail: xshfang@fudan.edu.cn; huangh@fudan.edu.cn; jianluwang@fudan.edu.cn